Viscous magnetization decrease in first-order reversal curves induced by rotatable magnetic anisotropy in polycrystalline exchange-biased bilayers

Maximilian Merkel,* Rico Huhnstock, Meike Reginka, Michael Vogel, and Arno Ehresmann
Institute of Physics and Center for Interdisciplinary Nanostructure Science and Technology (CINSaT), University of Kassel, Heinrich-Plett-Strasse 40, 34132 Kassel, Germany

Hubert Głowinski and Piotr Kuświk
Institute of Molecular Physics, Polish Academy of Sciences, Smoluchowskiego 17, 60-179 Poznań, Poland

(Received 14 July 2021; revised 6 September 2021; accepted 30 November 2021; published 6 December 2021)

A prototypical polycrystalline in-plane exchange bias system exhibited a viscous decrease of the ferromagnetic magnetization upon increasing external magnetic field when measuring first-order reversal curves. The phenomenon is investigated by means of angular-resolved vectorial magneto-optical Kerr magnetometry complemented by fits of model calculations and by Kerr microscopy. It is found that the viscous magnetization decrease is mediated by a rotatable magnetic anisotropy arising from thermally unstable antiferromagnetic grains coupled to the probed ferromagnet. This additionally manifests itself by a creeping domain wall motion in the ferromagnet due to thermally activated processes in the antiferromagnet. The investigations are in agreement with a generalized description of polycrystalline exchange bias systems and emphasize the relevance of understanding minor loop behavior addressing nonsaturated magnetic states for systems susceptible to dynamic changes on the hysteresis loop timescale.

DOI: 10.1103/PhysRevB.104.214406

I. INTRODUCTION

A standard way to investigate the macroscopic properties of a magnetic sample is to measure its hysteresis via recording the magnetization M as a function of an external magnetic field H from positive to negative saturation, i.e., to measure the so-called major magnetization loop. M represents the magnetization component equal to the projection of the magnetization vector $\vec{M}$ onto the direction of the external magnetic field $\vec{H}$. Hysteresis loops typically exhibit a monotonous decrease (increase) of the magnetization with decreasing (increasing) external field and can be characterized by two different switching fields H_{desc} and H_{asc} representing the zero-crossings of the respective branches for decreasing and increasing field, indicative for the coercive field $H_{\mathrm{C}} = (H_{\mathrm{asc}} - H_{\mathrm{desc}})/2$.

Whereas major loops depend on the global features of the magnetic sample [1,2], minor loops, not necessarily saturating the sample, enable to address different microscopic magnetic configurations of the probed specimen [2,3]. Such types of experiments are crucial to understand the dynamic magnetic response of a material in view of the growing operation speed of magnetic devices and the possible associated faster and nonsaturating cycling [2]. Measuring first-order reversal curves (FORCs) represents a systematic approach towards this goal, typically accompanied by a mathematically elaborated formalism [1–4]. One individual FORC is a magnetization curve measured starting from a positive external field H_{max} saturating the sample magnetically. Then the field is decreased down to a reversal field H_α, where the field gradient changes its sign and from which the field is again increased back to saturation. From H_α, the FORC depends on the external increasing driving field H with $H_\alpha \leqslant H \leqslant H_{\mathrm{max}}$ [1,3]. A set of minor loops with equidistant reversal fields between the saturating fields provides a complete set of FORCs $M(H_\alpha, H)$ as a magnetization matrix representing a subset of all accessible states enclosed by the major loop [1].

In contrast to the typically observed monotonous increase of the magnetization for increasing field [1,3,5–9], there have been observations of an anomalous viscous magnetization *decrease* (VMD) upon *increasing* driving field starting from nonsaturating $H_\alpha < 0$. This peculiar behavior has been observed in, e.g., $[\mathrm{CoFeB/Pd}]_n$- and $[\mathrm{Co/Pt}]_n$-multilayers with intrinsic perpendicular magnetic anisotropy [2,10,11] and CoFeB/Ta/CoFeB-trilayers as a synthetic antiferromagnet [12]. In these layer systems it is suggested that the physical origin of the VMD is a thermally activated propagation of domain walls overcoming their pinning barriers [2,10,12]. In systems composed of ferromagnetic nanograins embedded in a paramagnetic matrix, thermally activated relaxation resulting in a VMD or a decay of the magnetization at constant field was observed and generally explained assuming a distribution of energy barriers in the framework of the classical Preisach model [13]. Apart from systems with a magnetic anisotropy perpendicular to the sample plane, VMD has also been observed in in-plane exchange bias (EB) systems exhibiting a unidirectional magnetic anisotropy (UDA) manifesting itself as a horizontal shift $H_{\mathrm{EB}} = (H_{\mathrm{asc}} + H_{\mathrm{desc}})/2$ of the ferromagnetic hysteresis [14,15]. Either for a negative static nonsaturating field regarding NiFe/IrMn-bilayers [16] or upon increasing field starting from a nonsaturating $H_\alpha < 0$

*max.merkel@physik.uni-kassel.de

in the case of Co/Cu/IrMn-trilayers [17], a viscous decrease of the magnetization could be observed being promoted for decreasing $|H_{EB}|$ with $H_{EB} < 0$. Whereas in Ref. [16] it is concluded that the viscous decrease stems from the dynamically changing rotatable magnetic anisotropy (RMA) being present in polycrystalline EB systems [18–21], in Ref. [17] the VMD is correlated to a strong coupling between ferromagnetic entities, not necessarily excluding the former.

With the present study we want to contribute to the understanding of the described intriguing phenomenon in polycrystalline EB systems by evidencing the direct relation between the occurrence of the VMD and the RMA. In detail, we investigated IrMn/NiFe-bilayers as a prototypical polycrystalline EB system for different thicknesses of the antiferromagnetic (AF) and ferromagnetic (F) layer by measuring major loops and FORCs by means of longitudinal and vectorial magneto-optical Kerr magnetometry and Kerr microscopy. The prevailing magnetic anisotropies were disentangled by combining angular-resolved hysteresis measurements with an extended Stoner-Wohlfarth approach in the context of a model describing polycrystalline EB.

II. EXPERIMENTAL

A. Sample preparation

The prototypical EB bilayer of the type $Si(100)/Cu^{5\,nm}/Ir_{17}Mn_{83}^{t_{AF}}/Ni_{81}Fe_{19}^{t_F}/Si^{20\,nm}$ was fabricated on naturally oxidized Si using rf-sputter deposition at room temperature with an applied in-plane magnetic field set to 28 kA/m, where the base pressure was $<10^{-6}$ mbar and the working pressure $\approx 10^{-2}$ mbar, utilizing alloy targets with the same compositions given in the layer stack description. A 5 nm Cu buffer layer was used to induce a (111) texture in the $Ir_{17}Mn_{83}$ layer [20–22], while the 20 nm Si capping layer protects the underlying system from oxidation and enhances the contrast in the magneto-optical measurements [20,21,23]. For the AF $Ir_{17}Mn_{83}$ layer, thicknesses $t_{AF} = 5$ and 30 nm where chosen in order to promote the contribution of the RMA and the UDA, respectively [19,21,24,25], assuming columnar growth of the AF grains [21]. In the case of the F $Ni_{81}Fe_{19}$ layer, $t_F = 5, 7.5$, and 10 nm were chosen for scaling the exchange bias field H_{EB} and the coercivity H_C with the F layer thickness [24,26–29].

The layers were deposited using dc bias voltages set to $U_{Cu} = 600$ V, $U_{IrMn} = 700$ V, $U_{NiFe} = 600$ V, and $U_{Si} = 700$ V for which the deposition rates were determined to be $\eta_{Cu} = (6.8 \pm 0.3)$ nm/min, $\eta_{IrMn} = (6.0 \pm 0.3)$ nm/min, $\eta_{NiFe} = (4.30 \pm 0.15)$ nm/min, and $\eta_{Si} = (5.2 \pm 0.4)$ nm/min, respectively. For the determination of the rates the height profile of a calibration layer deposited on a substrate masked prior to the deposition was combined with its deposition time and the stated nominal layer thicknesses were set by choosing the times in accordance with the rates.

B. Magnetic characterization

The samples where magnetically characterized at room temperature by longitudinal and angular-resolved vectorial magneto-optic Kerr magnetometry (MOKE) as well as Kerr microscopy. For the longitudinal geometry (LMOKE) a setup was utilized where perpendicularly polarized light from a laser operating at a central wavelength of 632 nm is reflected from the sample with the sensitivity direction parallel to the external magnetic field and is analyzed via a combination of a detector and a polarizer adjusted with a difference of $\approx 90^\circ$ with respect to the initial polarization. In the case of angular-resolved vectorial MOKE (VMOKE) the setup described in Refs. [20,23] was used. For MOKE microscopy measurements an *evico magnetics* Kerr microscope was used, similar to the experiments in Refs. [29,30].

FORCs were obtained by LMOKE and exemplarily by Kerr microscopy measuring with the sensitivity direction and the external magnetic field parallel to the easy axis of the system. This axis is defined by the direction of the UDA of the EB layer system, initialized by depositing the layer system in an external magnetic field with an estimated uncertainty in the parallelity of deposition and measurement field of $\pm 1^\circ$. In the case of the LMOKE, the sweep rate $\nu \approx 2$ kA/m/s of the external magnetic field was kept constant throughout the FORC measurements and a resolution of $\Delta H \approx 0.05$ kA/m could be realized as the average difference between two measurement points. Regarding the Kerr microscope, a sweep rate of $\nu \approx 1.33$ kA/m/s and a resolution of $\Delta H \approx 0.08$ kA/m could be achieved. Angular-resolved magnetization curves were measured by the VMOKE setup as a function of the angle φ between the external magnetic field and the axis collinear to the sample's easy axis. With an increment of 1°, the angle was varied between $\varphi = 0^\circ$ and 360° and the magnetization curves shared a sweep rate of $\nu \approx 2.16$ kA/m/s and a resolution of $\Delta H \approx 0.33$ kA/m ($t_{Hys} \approx 92$ s).

III. POLYCRYSTALLINE MODEL

A. General description

The present study will be discussed within the scope of a description of polycrystalline EB systems [19–21,25,31–33] focusing on the interaction between the F layer and the granular AF, which is subdivided into grain classes of different thermal stability with respect to their averaged uncompensated magnetic moment at the AF/F-interface [25]. Each individual AF grain i possesses an energy barrier $\Delta E_{AF,i}$ between a global and a local energy minimum for the grain-averaged uncompensated interface magnetic moment $\vec{m}_{AF,i}$ relative to the orientation of the F magnetization $\vec{M}_F$ [31,32], which is in first order equal to the product $\Delta E_{AF,i} = K_{AF,i} V_{AF,i}$ of the anisotropy $K_{AF,i}$ and the volume $V_{AF,i}$ [20,32,34]. Assuming a constant K_{AF}, which might not be valid for small grain sizes [35], this allows to connect the distribution $\varrho(V_{AF})$ of grain volumes with the distribution of relaxation times $\tau_{AF,i} = \tau_0 \exp\{\Delta E_{AF,i}/k_B T\}$ between local and global energy minima, where $\nu_0 = 1/\tau_0$ represents the characteristic frequency for spin reversal of the AF grains, T the observation temperature, and k_B Boltzmann's constant [20,25,32,34]. Based on this, the distribution of relaxation times and likewise the distribution of grain sizes is subdivided into four different classes with different thermal stability for given measurement and storage temperatures as well as times [20,21,25].

Thermally unstable grains are subdivided into superparamagnetic (class I) and rotatable (class II) grains, where the latter possess relaxation times in the order of the hysteresis duration

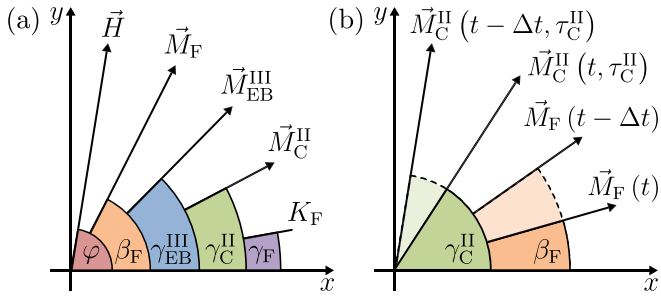

FIG. 1. (a) Angles corresponding to the relevant vectors in the model with respect to an arbitrary reference frame. $\vec{H}$ is the external magnetic field with its azimuthal angle φ, $\vec{M}_{\mathrm{F}}$ is the F magnetization with the angle β_{F}, K_{F} is the energy density of the FUMA with its easy direction defined by γ_{F}, $\vec{M}^{\mathrm{II}}_{\mathrm{C}}$ and $\vec{M}^{\mathrm{III}}_{\mathrm{EB}}$ are the superposed uncompensated magnetic moments related to AF grains of classes II and III with $\gamma^{\mathrm{II}}_{\mathrm{C}}$ and $\gamma^{\mathrm{III}}_{\mathrm{EB}}$ as the corresponding azimuthal angles connected to the RMA and the UDA, respectively. (b) Schematic of the RMA during a magnetization reversal of the F at time steps t and $t-\Delta t$ depicting the continuous relaxation of $\vec{M}^{\mathrm{II}}_{\mathrm{C}}$ into a state parallel to $\vec{M}_{\mathrm{F}}$.

t_{Hys}. The grain-averaged uncompensated magnetic moment of rotatable grains of class II at the AF/F-interface can rotate during remagnetization of the F and undergoes a relaxation process into a state parallel to the F magnetization. This mediates the coercivity H_{C} of the F layer, due to the necessity of overcoming the additional torque, resulting macroscopically in a RMA [18–21]. Thermally stable grains have relaxation times larger than t_{Hys} and are subdivided into grains of class III and IV, where class III grains can contribute to the exchange bias shift H_{EB} with a specific direction of a macroscopic UDA, as they can be set, e.g., during a post-annealing procedure (field cooling) [21,25,36], via ion bombardment [32,37–39] or via fabricating the EB system with additionally applying a sufficiently strong magnetic field during deposition [19,21,40]. AF grains, which cannot be set by either of these methods are accounted to class IV and their anisotropies are assumed to remain randomly distributed [20,25].

H_{EB} and H_{C} can be tuned by varying the deposition parameters of the AF layer, either scaling the lateral grain size [21,41,42], i.e., the mean grain radius assuming homogeneous columnar growth, or the thickness t_{AF} of the AF layer [4,25,36]. The proportion of H_{C} mediating grains contributing to class II and grains contributing to H_{EB} accounted to class III can be scaled with t_{AF} with the grain volume distribution passing the class boundary $V_{\mathrm{II/III}}$ between class II and III.

B. Stoner-Wohlfarth approach

For numerical calculations of magnetization curves and FORCs of polycrystalline EB systems the model introduced and applied in Refs. [20,21,23] for macroscopically describing polycrystalline EB bilayer systems will be utilized and further developed. The Stoner-Wohlfarth approach introduced in Ref. [20] assumes a coherent rotation of a uniform in-plane F magnetization during a remagnetization process and is represented by the free energy $E(\beta_{\mathrm{F}})$ of the F layer depending on its azimuthal angle β_{F} [Fig. 1(a)]. Via minimizing the energy interface density $E(\beta_{\mathrm{F}})/A$ with respect to the interface A using the perfect delay convention [20,21,43], β_{F} is calculated for varying external field strength H. The free energy is the sum of the F potential energy in the external magnetic field, its intrinsic anisotropy as well as two additional anisotropy terms representing the interaction of the F magnetization with superposed rotatable (class II) and fixed (class III) uncompensated AF moments. Due to the deposition in an external magnetic field the intrinsic anisotropy of the F layer of thickness t_{F} and saturation magnetization M_{S} is assumed to be uniaxial (FUMA) with an energy density K_{F} and an azimuthal angle γ_{F} parallel to the field applied during deposition [20]. The interaction of the uniform F magnetization with the polycrystalline AF layer can generally be represented by the energy area density [19,20]

$$-\sum_i J_i \frac{A_{\mathrm{AF},i}}{A}\cos(\beta_{\mathrm{F}}(t)-\beta_{\mathrm{AF},i}(t,\tau_{\mathrm{AF},i})) \tag{1}$$

with the granular exchange energy area density J_i between the F and an individual AF grain i with a relaxation time $\tau_{\mathrm{AF},i}$ sharing a contact interface $A_{\mathrm{AF},i}$ as well as the azimuthal angle $\beta_{\mathrm{AF},i}$ of the grain-averaged interface magnetic moment $\vec{m}_{\mathrm{AF},i}$. Each term of the sum in Eq. (1) corresponds to the exchange interaction of an individual AF grain with the F and is weighted by the proportion of the shared contact interface with respect to the whole interface A. It is now assumed, that the interaction of the uniform F with the AF grains of the contributing classes II and III can be condensed to the interaction of the F with the superposed uncompensated magnetic moments of the particular grain class

$$\vec{M}^{\mathrm{II/III}}_{\mathrm{C/EB}} = \sum_i \vec{m}^{\mathrm{II/III}}_{\mathrm{AF},i} \tag{2}$$

as the vector sum of the individual grain-averaged magnetic moments $\vec{m}^{\mathrm{II/III}}_{\mathrm{AF},i}$, with the azimuths $\gamma^{\mathrm{II}}_{\mathrm{C}}$ and $\gamma^{\mathrm{III}}_{\mathrm{EB}}$, corresponding to macroscopic unidirectional anisotropies induced into the F. Hence, supposing a constant $J = J_i\,\forall\, i$, Eq. (1) can be rewritten as two macroscopic energy area densities with the prefactors $J_{\mathrm{eff}}\, p_{\mathrm{II/III}}$ representing the product between the effective exchange energy density J_{eff} and the proportions $p_{\mathrm{II/III}}$ of AF grains accounted to class II and III with respect to the subset of AF grains contributing to the EB at all ($p_{\mathrm{II}} + p_{\mathrm{III}} = 1$). The effective exchange energy density $J_{\mathrm{eff}} = \xi\, p J$ is defined as the product of J, the proportion $p = (A_{\mathrm{II}} + A_{\mathrm{III}})/A$ of all interface areas belonging to AF grains of classes II (A_{II}) and III (A_{III}) with respect to the whole interface area A and a factor ξ considering a reduction of the coupling at the AF/F-interface, e.g., due to roughness, compensated moments or stoichiometric gradients. Thus, $p_{\mathrm{II/III}}$ can be written as $p_{\mathrm{II/III}} = A_{\mathrm{II/III}}/(A_{\mathrm{II}} + A_{\mathrm{III}})$. Based on this, the free energy area density of the F is given by [20,21]

$$\begin{aligned}\frac{E(\beta_F(t))}{A} =& -\mu_0 H M_{\mathrm{S}} t_{\mathrm{F}} \cos(\beta_{\mathrm{F}}(t)-\varphi)\\ &+ K_{\mathrm{F}} t_{\mathrm{F}} \sin^2(\beta_{\mathrm{F}}(t)-\gamma_{\mathrm{F}})\\ &- J_{\mathrm{eff}}\big[p_{\mathrm{II}}\cos\big(\beta_{\mathrm{F}}(t)-\gamma^{\mathrm{II}}_{\mathrm{C}}(t,\tau^{\mathrm{II}}_{\mathrm{C}})\big)\\ &+ p_{\mathrm{III}}\cos\big(\beta_{\mathrm{F}}(t)-\gamma^{\mathrm{III}}_{\mathrm{EB}}\big)\big]\end{aligned} \tag{3}$$

with μ_0 as the magnetic permeability in vacuum. For modeling the time-dependent contribution of the thermally unstable

TABLE I. Values for $|H_{EB}|$ and H_C for the investigated samples A–F with different t_F and t_{AF} ($\varphi \approx 0°$). The uniaxial anisotropy constant K_F, the effective exchange energy area density J_{eff}, the proportion p_{III} of AF grains accounted to class III and the average relaxation time τ_C^{II} of class II grains were determined by fitting model calculations to measured angular-resolved dependencies $H_{EB/C}(\varphi)$. For the simulations of FORCs (Sim.) the used parameters for t_F, K_F, J_{eff}, p_{III}, and τ_C^{II} are given.

Sample	t_F (nm)	t_{AF} (nm)	$\lvert H_{EB}\rvert$ $\left(\frac{kA}{m}\right)$	H_C $\left(\frac{kA}{m}\right)$	K_F $\left(\frac{kJ}{m^3}\right)$	J_{eff} $\left(10^{-5}\,\frac{J}{m^2}\right)$	p_{III}	τ_C^{II} $(10^{-3}\,t_{Hys})$
A	5	5	2.69 ± 0.13	11.48 ± 0.13	2.38 ± 0.53	6.68 ± 0.01	0.18 ± 0.03	5.3 ± 1.5
B	5	30	13.73 ± 0.10	4.77 ± 0.09	1.83 ± 0.04	7.20 ± 0.01	0.72 ± 0.01	2.9 ± 1.2
C	7.5	5	1.46 ± 0.02	7.61 ± 0.02	2.80 ± 0.12	4.32 ± 0.05	0.32 ± 0.13	7.0 ± 2.4
D	7.5	30	7.87 ± 0.02	2.65 ± 0.02	0.92 ± 0.10	4.89 ± 0.01	0.85 ± 0.03	3.3 ± 1.2
E	10	5	1.52 ± 0.11	5.35 ± 0.11	2.13 ± 0.28	3.01 ± 0.01	0.35 ± 0.16	7.8 ± 2.5
F	10	30	5.81 ± 0.12	1.95 ± 0.12	0.67 ± 0.10	4.82 ± 0.25	0.87 ± 0.01	3.5 ± 1.3
Sim.	7.5				{0, 0.5, 2}	4	{0.25, 0.8}	5

grains as a continuous relaxation of the superposed uncompensated moment of class II, the azimuthal angle of the RMA is defined as [31]

$$\gamma_C^{II}\left(t, \tau_C^{II}\right) = \beta_F(t - \Delta t)\left(1 - \exp\left\{-\Delta t/\tau_C^{II}\right\}\right) + \gamma_C^{II}\left(t - \Delta t, \tau_C^{II}\right)\exp\left\{-\Delta t/\tau_C^{II}\right\} \quad (4)$$

with the average relaxation time τ_C^{II} of all rotatable grains of class II. For each step during the remagnetization of the F, for which $\beta_F(t)$ is determined, $\gamma_C^{II}(t, \tau_C^{II})$ is derived from the history of the F and the RMA at $t - \Delta t$ and is as β_F set equal to φ at initial positive saturation.

IV. RESULTS AND DISCUSSION

A. Macroscopic magnetic characterization

In Table I the macroscopic characteristics of the AF/F-bilayer samples (named A–F), the absolute value of the exchange bias shift $|H_{EB}|$ and the coercivitiy H_C, are given for $t_F = 5$, 7.5, and 10 nm and $t_{AF} = 5$ and 30 nm derived from LMOKE measurements with respect to the easy axes ($\varphi \approx 0°$). For increasing t_F and fixed t_{AF}, $|H_{EB}|$ and H_C follow within the uncertainties an inversely proportional dependence on t_F [24,26–28]. For fixed t_F, H_C and H_{EB} exchange their strengths when AF layer thicknesses of $t_{AF} = 5$ and 30 nm are compared, due to a comparably stronger RMA for $t_{AF} = 5$ nm and a stronger UDA for $t_{AF} = 30$ nm [19,21,24,25].

In order to quantitatively retrieve model parameters (Table I) utilizing the model of Refs. [20,21,23], calculations were fitted to measured angular-resolved dependencies $H_{EB/C}(\varphi)$. The azimuthal angles γ_F and γ_{EB}^{III} of the FUMA and the UDA were not kept constant or set to zero but showed no significant trend and the difference $|\gamma_F - \gamma_{EB}^{III}|$ could be determined to be below 2°. For $t_F = 10$ nm and $t_{AF} = 5$ and 30 nm the utilized saturation magnetization $M_S = 686 \pm 8$ kA/m of the investigated F was obtained by using a vector network analyzer ferromagnetic resonance spectrometer.

For fixed t_F, p_{III} is smaller (larger $p_{II} = 1 - p_{III}$) for $t_{AF} = 5$ nm in comparison to $t_{AF} = 30$ nm visible by the observed decrease of $|H_{EB}|$ (increase of H_C). This demonstrates the tunability of the amount of grains that can be accounted to class II or III via changing t_{AF}. Likewise, J_{eff} is decreased for the thinner AF layer, due to the decrease of the amount of AF grains contributing either to class II or III, i.e., the reduction of contributing coupling sites $p = (A_{II} + A_{III})/A$. In contrast, K_F and τ_C^{II} are increased for $t_{AF} = 5$ nm. It is assumed, that in the case of large p_{III}, the continuous relaxation of rotatable grains into the direction of the F magnetization is suppressed for large grains of class II, because the RMA can only follow M_F if the F remagnetizes. The F is expected to stay saturated by pinning via AF grains of class III in the vicinity of class II grains. This results in an effective reduction of the grain class boundary between thermally stable and thermally unstable grains and hence in a reduction of τ_C^{II}. For small p_{III} the pinning by thermally stable grains is reduced and the change of the F magnetization with respect to the fixed UDA is promoted. It is important to point out, that this also depends on the intrinsic remagnetization behavior of the investigated F. Regarding K_F, the strength of the intrinsic uniaxial anisotropy is expected to be overestimated by the model, due to the increase of H_C, revealing a limitation of the applied coherent rotation approach, since the formation of domains in the F is excluded per definition [17,20].

For fixed t_{AF} and increasing t_F, the determined values for J_{eff} tend to be smaller, while p_{III} and τ_C^{II} are bigger. This suggests a larger coupling at the AF/F-interface for thinner F, due to an inversely proportional dependence of J_{eff} on t_F as for H_C and H_{EB}. A stronger coupling at the interface promotes RMA in comparison to UDA and furthermore decreases on average the energy barrier of AF grains for changing their state with respect to the F magnetization, which results in a larger contribution of class II grains (decrease of p_{III}) but also a decrease of τ_C^{II} for decreasing t_F and fixed t_{AF} [19,31,32].

The determined model parameters given in Table I shall serve for highlighting the choice of investigated layer thicknesses and especially the clear promotion of RMA and UDA for $t_{AF} = 5$ and 30 nm, respectively, as well as a starting point for simulating the FORCs.

B. FORC analysis and viscous magnetization decrease (VMD)

Kerr microscopy. For sample E ($t_F = 10$ nm and $t_{AF} = 5$ nm) a major loop and two representative FORCs starting from reversal fields $H_\alpha = -5.24$ and -5 kA/m, respectively, are exemplarily depicted in Fig. 2(a) for $\varphi \approx 0°$. The measurement angle is indicative for the external magnetic field being parallel to the induced UDA ($\varphi \approx \gamma_{EB}^{III}$). The major loop of the *longitudinal* (∥) magnetization component has

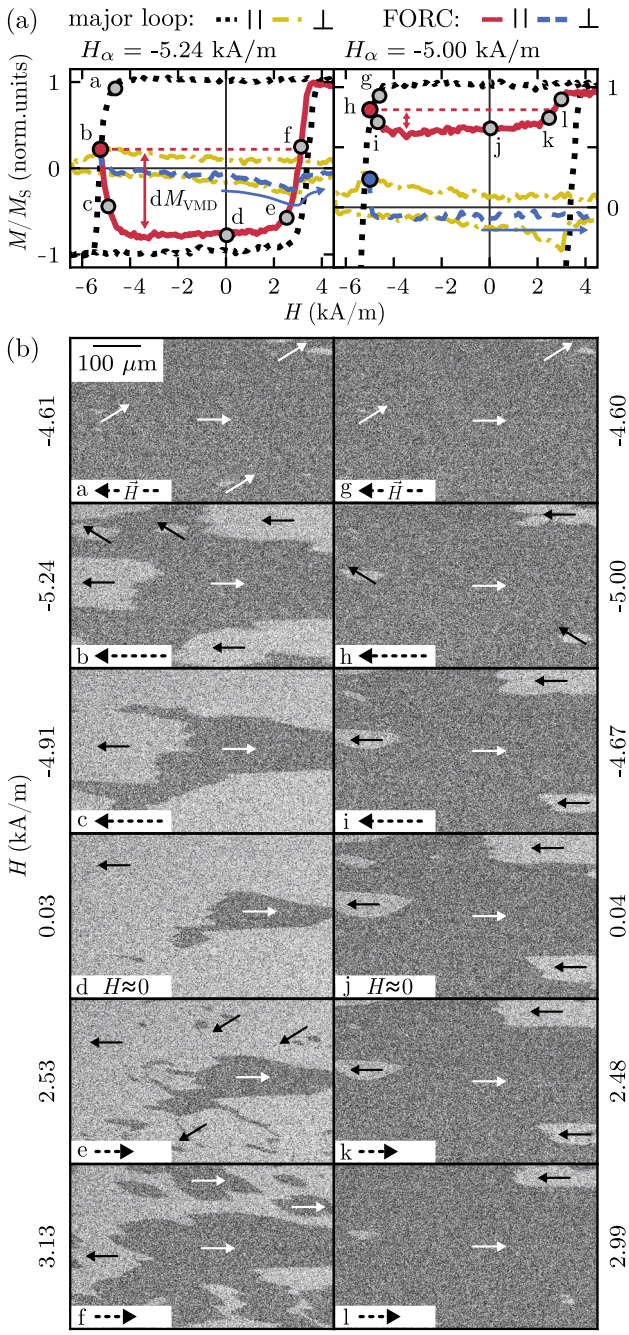

FIG. 2. (a) Exemplary *longitudinal* (∥) and *transversal* (⊥) FORCs of sample E measured by Kerr microscopy and VMOKE for $H_\alpha = -5.24$ and –5 kA/m and $\varphi \approx 0°$ in comparison to the respective components of the major loop. The longitudinal magnetization at the reversal field H_α is indicated with a dashed line parallel to the figure's abscissa crossing its ordinate. Note the different ordinates of the two panels. (b) Domain configurations observed by Kerr microscopy are shown for external fields indicated at the sides of panels a - f for the FORC with reversal field $H_\alpha = -5.24$ kA/m and panels g to l for $H_\alpha = -5$ kA/m. Panels b and h correspond to H_α. White (→) and black (←) arrows represent positive and negative longitudinal magnetization, respectively.

been obtained via Kerr microscopy. The *transversal* (⊥) magnetization component has been determined by vectorial MOKE magnetometry (VMOKE) under comparable experimental conditions as the Kerr microscopy measurements. Kerr microscopy images at specific field steps with respect to both FORCs are presented in Fig. 2(b).

For the major loop it can be observed, that as the longitudinal component starts to decrease for the decreasing branch, the transversal component increases showing a peak slightly below the zero-crossings of the hysteresis, decreasing to zero as the longitudinal component fully reverses [Fig. 2(a)]. This indicates a rotation of the magnetization of nucleated domains away from the original orientation as it is schematically indicated in the Kerr-microscopy images in Fig. 2(b) a and g followed by an abrupt change of the longitudinal components direction [Fig. 2(b) b and h] and further by a continuous decrease of the transversal component as the domains align with respect to the negative external magnetic field.

Following the paths of the FORCs for both negative nonsaturating H_α, a viscous *decrease* of the *longitudinal* (∥) component can be observed upon *increasing* external magnetic field ($dH > 0$ kA/m). For increasing H from H_α, the magnetization decreases by $dM_{VMD}(H_\alpha)$ [Fig. 2(a)] until it stabilizes in between a certain field range showing a nonzero magnetization between the starting value at H_α and negative saturation. For both H_α, the *transversal* (⊥) component follows the transversal major loop down to H_α for decreasing H and decreases under increasing H, similar to the longitudinal component, but decreases to zero after significantly fewer field steps in comparison to the stabilization of the longitudinal component. Comparing the Kerr microscopy images at $H_\alpha = -5.24$ and -5 kA/m in Fig. 2(b) b and h with the images at $H = -4.91$ and -4.67 kA/m in Fig. 2(b) c and i, located on intermediate steps during the course of the VMD where the transversal component already decreased to zero, it can be concluded, that the magnetization *decrease* under *increase* of H is dominated by domain wall movement connected to an increase of already nucleated domains. The domains increase until a stable multidomain state has developed for -4 kA/m $\lesssim H \lesssim 0$ kA/m as shown in Fig. 2(b) d and j for $H \approx 0$ kA/m.

In the case of $H_\alpha = -5$ kA/m, where the macroscopic longitudinal magnetization does not decrease below zero, the domains, which increased during the VMD, gradually shrink via domain wall movement for increasing H from $H = 0$ kA/m [Fig. 2(b) j → k → l], without a detectable transversal component [Fig. 2(a)]. Contrarily, for $H_\alpha = -5.24$ kA/m, where the longitudinal magnetization decreases from a positive to a negative value near saturation, remagnetization incorporating a transversal component can be observed [Fig. 2(a)]. This is connected to the nucleation of positive domains, dominating the reversal of the longitudinal component to positive saturation for $H_\alpha = -5.24$ kA/m, whereas for $H_\alpha = -5$ kA/m the reversal is dominated by domain wall movement connected to the shrinking of negative domains.

Based on Ref. [12] and the exemplary Kerr-microscope and VMOKE investigations of sample E with respect to representative FORCs (Fig. 2), different types of domains taking part in the remagnetization can be identified:

(i) Domains, which are formed under decreasing H down to H_α are called ***retained*** domains, showing negative longitudinal magnetization with respect to the initial

positive saturation, remaining in the sample as H is increased from H_α. Those domains either *increase* via domain wall propagation during increasing $H < 0$ kA/m ($\mathrm{d}H > 0$ kA/m) and even merge for large $|H_\alpha|$ or *decrease* again via domain wall movement for $H > 0$ kA/m.

(ii) ***Reversal*** domains nucleate upon increasing H from H_α showing either negative or positive magnetization depending on whether they are created during the VMD or during the macroscopic magnetization increase from the stable multidomain state to positive saturation.

The point in time at which a specific domain is nucleated determines whether it is classified as a *retained* or as a *reversal* domain. *Retained* domains are formed before and *reversal* domains nucleate after H_α. Thus, considering a single FORC measured in between $H_\alpha \leqslant H \leqslant H_{\max}$, *retained* domains are already present, whereas *reversal* domains nucleate during the course of the FORC.

FORC analysis. Based on the exemplary investigation of minor loops exhibiting VMD for $t_\mathrm{F} = 10$ nm and $t_\mathrm{AF} = 5$ nm (sample E), a systematic approach to measure minor loops for varying t_AF and t_F is given by the FORC formalism. This serves as a mapping method for the distribution of microscopic coercivities and interaction fields of the respective sample [2,4]. Despite the fact that the interpretation of FORC distributions is in most cases not straightforward if the formalism is applied as a stand-alone technique, the formalism was already applied to a variety of magnetic systems [1,3,4,8,12,44–46]. However, the correlation of features observable in FORC distributions to physical properties can be facilitated if combined with other methods and theoretical models comparable to experimental observations [3,12,46–48].

The FORC distribution is defined as the mixed second derivative

$$\mu(H_\alpha, H) = -\frac{\partial^2 M(H_\alpha, H)}{\partial H_\alpha \partial H} \quad \text{with} \quad H_\alpha \leqslant H \tag{5}$$

and commonly the coordinates $\{H_\alpha, H\}$ are transformed to $H_\mathrm{c} = (H_\alpha - H)/2$ and$H_\mathrm{i} = (H_\alpha + H)/2$ [3] resulting in rotating the FORC distribution counterclockwise by 45°. It yields a distribution $\mu(H_\mathrm{i}, H_\mathrm{c})$ of coercivities H_c and interaction fields H_i representative for the individual contributions of the polycrystalline system [1,3]. H_c and H_i should not be misunderstood with the coercivity H_C and the horizontal exchange bias shift H_EB as macroscopic characteristics of the F major loop.

For the actual determination of the FORC distribution via evaluating Eq. (5), a second-order polynomial

$$M_\mathrm{fit}(H_\alpha, H) = c_0 + \sum_{i=1}^{2} \alpha_i {H_\alpha}^i + \sum_{i=1}^{2} \beta_i H^i - \mu_{H_\alpha, H} H_\alpha H \tag{6}$$

is fitted to the set of FORCs $M(H_\alpha, H)$ with the fit parameters α_i, β_i for $i \in \{1, 2\}$ and c_0 as well as $\mu_{H_\alpha, H}$, representing the FORC distribution $\mu(H_\alpha, H)$ [1]. The number of points N_fit taken into account for the fit is determined via a smoothing factor SF such that $N_\mathrm{fit} = (2\,\mathrm{SF} + 1)^2$ sampling points are used representing the N_fit nearest neighbours of the point (H_α, H) in the triangular FORC space spanned by H_α and H [1]. The least squares of the fit are weighted with respect to their distance using

$$w_j = \left(1 - \left[\frac{|\vec{h} - \vec{h}_j|}{\max_j |\vec{h} - \vec{h}_j|}\right]^3\right)^3 \tag{7}$$

with $j \in \{1, \ldots, N_\mathrm{fit}\}$ in order to realize a meaningful approximation of $M(H_\alpha, H)$ with Eq. (6) in the case of an irregular non-equidistant grid [1,49]. $\vec{h}$ represents the point (H_α, H) where $\mu(H_\alpha, H)$ shall be determined and $\vec{h}_j$ defines the positions of the sampling points for the least squares fit.

In Fig. 3, FORCs $M(H_\alpha, H)$ and respective distributions $\mu(H_\mathrm{i}, H_\mathrm{u})$ are presented for samples with $t_\mathrm{F} = 5$, 7.5, and 10 nm and $t_\mathrm{AF} = 5$ and 30 nm and $\varphi \approx 0°$, determined by LMOKE. $\mu(H_\alpha, H)$ was in all cases determined using SF = 10 as a compromise between signal removal and noise reduction [1]. For the transformation $\{H_\alpha, H\} \rightarrow \{H_\mathrm{i}, H_\mathrm{c}\}$ and representation of $\mu(H_\mathrm{i}, H_\mathrm{c})$ the irregular grid was interpolated with an increment of 0.05 kA/m for both coordinates. For further noise reduction a Gaussian filter was applied with 2.5 kA/m as the standard deviation for the Gaussian kernel.

For $t_\mathrm{AF} = 5$ nm and all t_F [Figs. 3(a), 3(c), and 3(e)], a VMD under increasing H is observable, which is suppressed for $t_\mathrm{AF} = 30$ nm [Figs. 3(b), 3(d), and 3(f)] and t_F approaching 5 nm [Fig. 3(a)]. In the FORC diagrams, identifiable features are labeled with M and N for $t_\mathrm{AF} = 5$ nm [Figs. 3(g), 3(i), and 3(k)] and with O for $t_\mathrm{AF} = 30$ nm [Figs. 3(h), 3(j), and 3(l)] shared by all t_F with M and O located at H_i and H_c in the proximity of H_EB and H_C of the corresponding major loop. N is located at negative H_i close to the zero-crossing of the decreasing branch of the major loop and close to zero H_c, consisting of a negative peak followed by a positive one for decreasing H_i. Comparing $M(H_\alpha, H)$ with the determined distributions $\mu(H_\mathrm{i}, H_\mathrm{c})$, M and O can be associated to remagnetization processes connected to an increasing magnetization connected either to the nucleation of *reversal* or the shrinking of *retained* domains, whereas N is connected to VMD observable for $t_\mathrm{AF} = 5$ nm upon increasing field.

As for $t_\mathrm{F} = 10$ nm in Figs. 3(k) and 3(l) the peaks regarding M, N, and O are well observable and of comparable width, an overall broadening of the spots connected to M and O can be observed for decreasing t_F [Figs. 3(g)–3(j)]. In contrast, N does not change significantly by changing t_F, besides its position and peak heights in comparison to M. This indicates, that N and consequently the VMD is mainly depending on the properties of the thin AF layer, whereas the residual observed remagnetization processes depend on the interaction occurring at the AF/F-interface and/or on the intrinsic properties of the F. The broadening of the M and O peak for decreasing t_F along the diagonal H axis, arises from a broadening of the distribution of switching fields connected to the nucleation of *reversal* domains and the domination of nucleation over domain wall movement [12]. Based on Fig. 2(b) for $t_\mathrm{F} = 10$ nm and $t_\mathrm{AF} = 5$ nm, Kerr microscopy images showed that whether the nucleation of *reversal* domains dominates domain wall motion of *retained* domains for positive increasing H depends on the initial state $M(H_\alpha)$ of the individual FORC, the amount of magnetization decrease $\mathrm{d}M_\mathrm{VMD}(H_\alpha)$ [Fig. 2(a)]

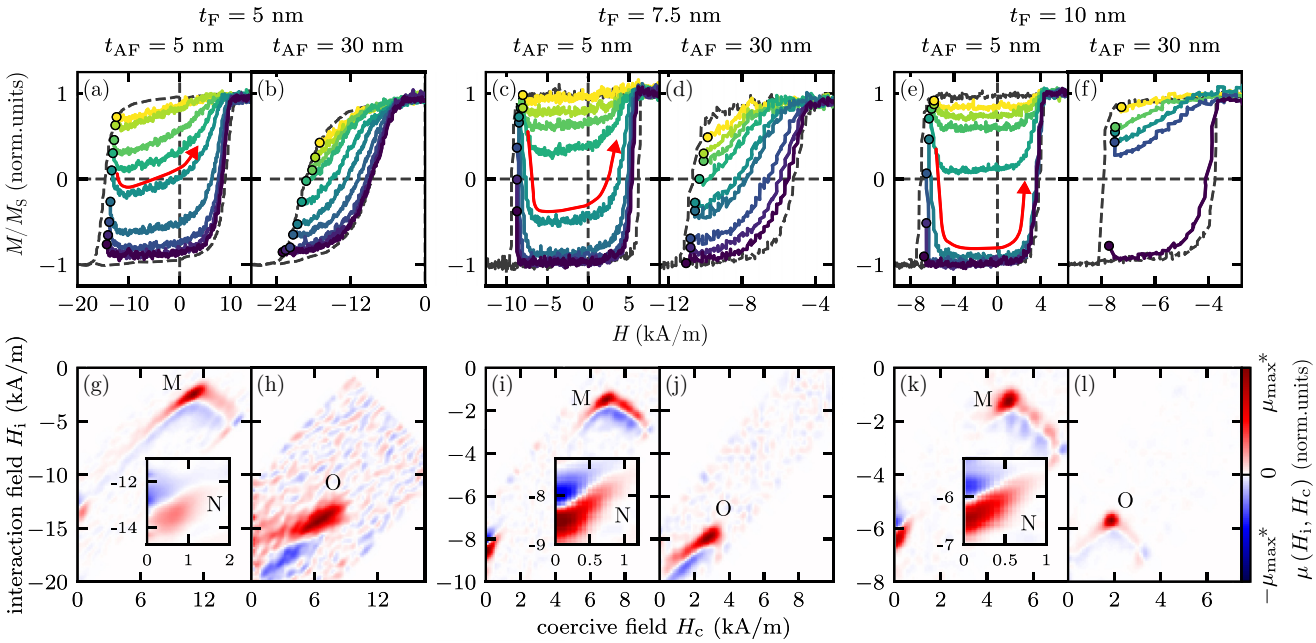

FIG. 3. FORCs $M(H_\alpha, H)$ [(a)–(f)] measured along the systems' easy axes ($\varphi \approx 0°$) and corresponding FORC distributions $\mu(H_i, H_c)$ [(g)–(l)] of interaction fields H_i and coercive fields H_c. Colours are guides to the eye for differentiating individual FORCs with respect to H_α. For the sake of visibility, only representative FORCs with H_α in the vicinity of the zero-crossing of the major loop are shown. Red arrows exemplarily indicate the magnetization path of FORCs showing VMD. Identifiable features shared by the FORC distributions are labeled by M, N and O, and the color scale of the distribution maps is normalized to the maximum $\mu_{max}{}^*$ of the peaks denoted by M or O.

and whether the magnetization changes sign. The comparable width of spot M with respect to H_i and H_c for $t_F = 10$ nm [Fig. 3(k)] suggests that the dominance of nucleation and the dominance of domain wall propagation is equally separated by a specific H_α, which is not given for lower t_F [Figs. 3(g) and 3(i)]. The proximity of N to zero H_c for $t_{AF} = 5$ nm and all t_F [Figs. 3(g), 3(i), and 3(k)] indicates, that *retained* domains growing in size during the VMD are primarily created until H_α is reached, and that the VMD is dominated by domain wall propagation (Fig. 2) [12].

$\mu(H_i, H_c)$ is often interpreted as a well-defined distribution and is expected to be of positive sign, which is only valid if minor loops are congruent and close after a field cycle [46,50]. Those criteria are in most cases not fulfilled, particularly for systems featuring interaction effects [46]. This is the case for the investigated AF/F-bilayer system where the interaction between the layers can only indirectly be investigated. Moreover, thermally activated changes in the AF layer are highly sensitive to measurement conditions and field paths [16]. Besides utilizing the FORC analysis solely as a method fingerprinting the microscopic magnetic properties [4,46], $\mu(H_i, H_c)$ or rather $\mu(H_\alpha, H)$ can also be interpreted as a measure of the change of the magnetic susceptibility $\chi = \partial M(H_\alpha, H)/\partial H$, representing the slope of the FORCs for a specific H_α. Here, a positive sign of the distribution corresponds to a decrease of χ [see Eq. (5)] [12]. Hence, a negative sign of $\mu(H_\alpha, H)$ is connected to an increase of χ. It is visible in the FORCs showing VMD for $t_{AF} = 5$ nm in Figs. 3(a), 3(c), and 3(e), that in the case of increasing H_α firstly a decrease of the slope can be observed, due to the *decreasing* magnetization upon *increasing* field in contrast to a monotonous magnetization increase starting from negative saturation. For further increasing H_α the slope increases possessing a negative value, which results in the characteristic structure of the N peak with a positive peak followed by a negative one in the proximity of zero H_c for increasing H_α. Consequently, as observed in Fig. 2, less or smaller *retained* domains are present at H_α for increasing H_α and therefore the absolute value of χ decreases regarding the VMD. For the spots M and O it can be observed vice versa, where for increasing H_α a certain range of reversal fields results in an increase of the positive χ followed by a decrease of the slope for further increasing H_α. This corresponds to a decrease of the field H for increasing H_α from which *retained* domains are remagnetized via the nucleation of *reversal* domains (Supplemental Material of Ref. [12]).

Viscous magnetization decrease (VMD) induced by the rotatable magnetic anisotropy (RMA). From the experimental observations of FORCs in the studied prototypical AF/F-bilayer system it is evidenced that the VMD is a process induced by the RMA dominating the unidirectional anisotropy (UDA) of the system with the RMA exhibiting a larger energy area density (Table I). The VMD is based on thermally activated processes in the AF resulting in an ongoing domain wall propagation in the F under increasing H if the system had been driven from positive saturation to a negative reversal field [16]. Due to the dynamic changes of thermally unstable AF grains mediating the macroscopic RMA, they adapt during the remagnetization of the F until H_α is reached and stabilize the *retained* domains nucleated before. This may be described by an effective field acting on the F, which decreases during the VMD upon the increasing external driving field, if H_{EB} is already compensated. As the alignment of class II grains in contact to *retained* domains saturates, a stable multidomain

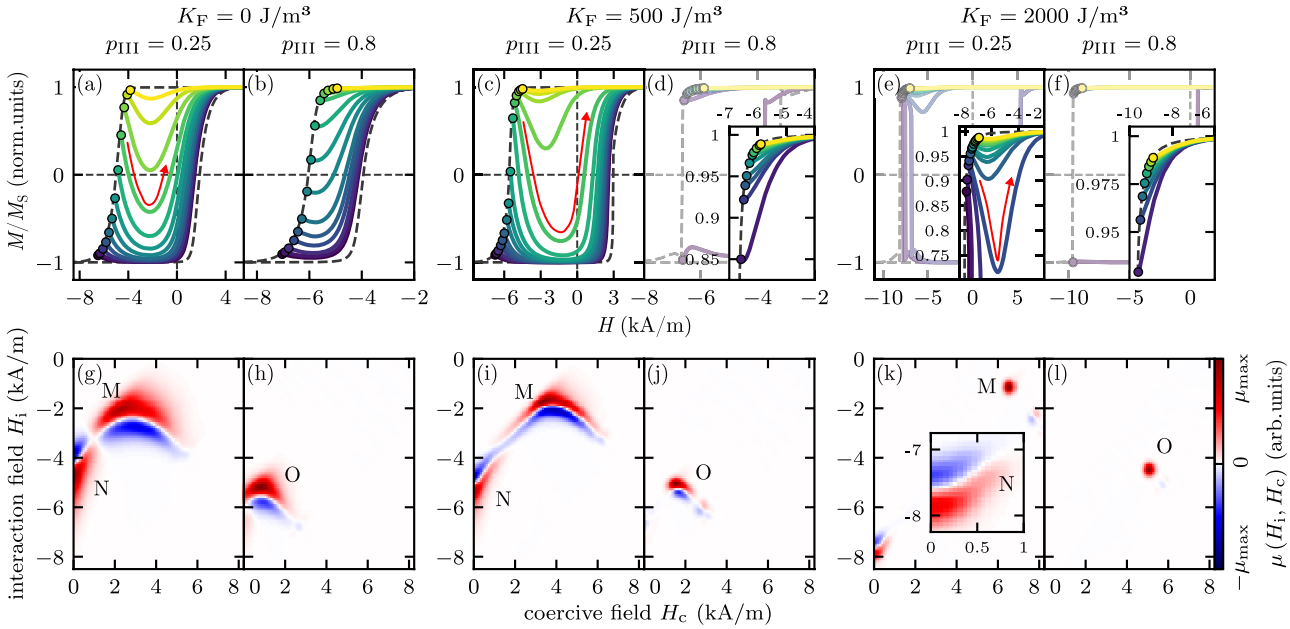

FIG. 4. FORCs $M(H_\alpha, H)$ [(a)–(f)] simulated for $\varphi = 1^\circ$ and $t_F = 7.5$ nm as well as corresponding FORC distributions $\mu(H_i, H_c)$ [(g)–(l)] of interaction fields H_i and coercive fields H_c. Colours are guides to the eye for differentiating individual FORCs with respect to H_α. For the sake of visibility, only representative FORCs with H_α in the vicinity of the zero-crossing of the major loop are shown. Red arrows exemplarily indicate the magnetization path of FORCs showing VMD. Identifiable features shared by the FORC distributions are denoted by M, N, and O as in Fig. 3, and the color scale of the distribution maps is normalized to the maximum value of the distributions μ_{max}.

state is reached. The F remagnetizes back to positive saturation for sufficient H either by shrinking of *retained* domains via domain wall motion or by the creation of *reversal* domains. Which of the two mechanisms dominates depends on how many RMA mediating AF grains are already aligned with *retained* domains. This in turn depends on H_α and explains the change of the magnetic susceptibility in the FORC diagrams [Figs. 3(g), 3(i), and 3(k)] for increasing reversal field H_α.

The stronger VMD compared to the one in Ref. [17] is possibly caused by having used NiFe in direct contact with the AF, whereas in Ref. [17] the F Co has been separated by a Cu spacer from the AF. This reduces significantly the coupling between F and AF being crucial for the RMA.

C. FORC simulation

Simulations of FORCs were performed by the approach of Refs. [20,21] advanced by the additional implementation of a continuous RMA adapting to the F magnetization reversal depending on its own history [Eq. (4)]. The derived parameters from the model fit compared to experimental data of the investigated samples presented in Table I showed that the most significant changes in dependence of t_{AF} are given for K_F and for p_{III}. For a general comparison to the studied samples, those parameters were set to $K_F = 0, 0.5$ and 2 kJ/m^3 and in each case p_{III} was set to 0.25 and 0.8 (Table I). The other model parameters were chosen to be $J_{eff} = 4 \cdot 10^{-5}$ J/m^2, $\tau_C^{II} = 5 \cdot 10^{-3}\, t_{Hys}$, $t_F = 7.5$ nm, and $M_S = 686$ kA/m. The azimuthal angles of the UDA and the FUMA were set to $\gamma_F = \gamma_{EB}^{III} = 0^\circ$ and the angle of the external driving field was chosen to be $\varphi = 1^\circ$, to simulate a possible experimental misalignment. The resolution was set to $\Delta H = 0.05$ kA/m and the same parameters with respect to the determination of the FORC distributions were used as for the experimental investigations. The simulated FORCs and corresponding distributions are depicted in Fig. 4.

For $p_{III} = 0.25$ and all K_F [Figs. 4(a), 4(c), and 4(e)], a VMD is observable, which is either not significant or suppressed for $p_{III} = 0.8$ [Figs. 4(b), 4(d), and 4(f)]. The spots in the experimental FORC diagrams are qualitatively reproduced by the simulations and are labeled with M and N for $p_{III} = 0.25$ [Figs. 4(g), 4(i), and 4(k)] and with O for $p_{III} = 0.8$ [Figs. 4(h), 4(j), and 4(l)] shared by all K_F. For $K_F = 2$ kJ/m^3 the simulated FORC distributions $\mu(H_i, H_c)$ for $p_{III} = 0.25$ and 0.8 [Figs. 4(k) and 4(l)] reproduce best the distributions for $t_F = 10$ nm and $t_{AF} = 5$ and 30 nm [Figs. 3(k) and 3(l)], respectively. This is due to the well observable switching of the simulated magnetization to negative saturation under increasing field below a certain H_α [Fig. 4(e)]. Since the magnetization either reverses back to positive saturation after the VMD or stays negative before the final remagnetization, no strong widening of the labeled features can be observed in opposition to lower K_F [Figs. 4(g)–4(j)]. This holds true for the experimental FORC distributions determined for $t_F = 10$ nm [Figs. 3(k) and 3(l)], but is additionally correlated to the stable multidomain state after the VMD. Multidomain states, however, are excluded in the Stoner-Wohlfarth-type simulations per definition. For decreasing K_F, a broadening of the identified features can be observed [Figs. 4(g)–4(j)] as well as in the experimental FORC distributions for decreasing t_F [Figs. 3(g)–3(j)]. In the simulations this arises from an increasing contribution of coherent rotation to the magnetization reversal for decreasing intrinsic uniaxial anisotropy, continuously dragging the dynamically adapting RMA. For large K_F, a step-like magnetization reversal occurs due to the fast domain-wall motion dominated magnetization reversal. This

can be seen for $p_{\mathrm{III}} = 0.8$, where a fast magnetization reversal from $M(H_\alpha)$ to positive saturation is observed for large K_{F} [Fig. 4(f)] and a slower magnetization reversal for small K_{F} [Fig. 4(b)].

The comparison of the experimentally determined (Fig. 3) and the simulated (Fig. 4) FORCs and corresponding distributions demonstrates, that the inclusion of the RMA and obeying the magnetic history of the sample in the simulations enables to qualitatively reproduce the relevant features of the FORC distributions as well as the VMD for varying t_{F} and t_{AF}. Two essential limitations of the model, however, hamper a quantitative reproduction. One is the coherent rotation of the uniform F magnetization, disabling the description of interactions between different F sites with different local anisotropies, and, correspondingly, the formation of multidomain states. This challenge might be solvable by a granular-like approach as in Refs. [17,51]. The second is the significant entanglement between the FUMA and the RMA within the current model (Table I). Comparing $t_{\mathrm{AF}} = 5$ and 30 nm, an increase of RMA results in an increase of K_{F}. Additionally, for $t_{\mathrm{AF}} = 30$ nm, K_{F} increases significantly for decreasing t_{F}, whereas for $t_{\mathrm{AF}} = 5$ nm only an overall trend for an increasing K_{F} for decreasing t_{F} can be observed, which is for $t_{\mathrm{F}} = 5$ nm within the determined uncertainties. A stronger RMA for decreasing t_{F} results in an increase of K_{F} in the applied model. Furthermore, a decrease of t_{F} yields experimental FORC distributions with widened peaks, which is in the simulations correlated to an increased influence of the coherent rotation of the F magnetization reversal. For an individual F layer, smaller t_{F} might result in a reduction of the intrinsic FUMA [52]. For NiFe this effect is superimposed by an increase of the FUMA due to the interaction with RMA mediating AF grains. This might explain the dependence of K_{F} on t_{AF} and t_{F} derived by the model fit and also the change of the experimental FORC distributions for decreasing t_{F}.

D. Measures for VMD

Based on Ref. [2], we define by

$$\mathrm{d}M_{\mathrm{VMD}}(H_\alpha) = M(H_\alpha) - \min_{H_\beta} M(H_\alpha, H_\beta) \tag{8}$$

a quantitative measure for the VMD strength as the difference between the initial magnetization $M(H_\alpha)$ and the minimum magnetization value in an individual FORC [Fig. 2(a)]. $\mathrm{d}M_{\mathrm{VMD}}(H_\alpha)/2$ represents the area proportion of domains reverted with respect to the saturation magnetization accumulated during the VMD in comparison to the magnetic state at H_α. This corresponds to the area gained by domains via nucleation and domain wall movement in proportion to the investigated sample section. This measure as a function of H_α is shown in Fig. 5 for $t_{\mathrm{AF}} = 5$ nm and $t_{\mathrm{F}} = 5$, 7.5, and 10 nm. In the same figure the integrated distribution of interaction fields $\mu(H_{\mathrm{i}})$ based on Figs. 3(g), 3(i), and 3(k) are displayed. The $\mathrm{d}M_{\mathrm{VMD}}(H_\alpha)/2$ for different t_{F} show a clear peak at reversal fields corresponding to the centres of $\mu(H_{\mathrm{i}})$.

The maximum strength of the VMD $\mathrm{d}M^{\mathrm{max}}_{\mathrm{VMD}} = \max_{H_\alpha}\{\mathrm{d}M_{\mathrm{VMD}}(H_\alpha)\}$ can be derived directly, whereas for the determination of the full width at half maximum ΔH_α and the peak area $\mathcal{A}$, Lorentzian functions

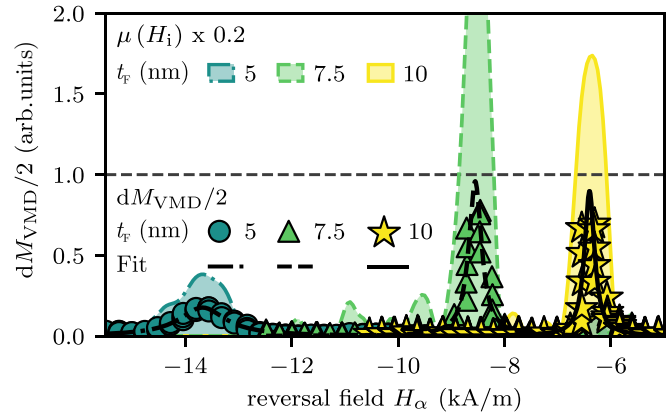

FIG. 5. $\mathrm{d}M_{\mathrm{VMD}}/2$ for samples A, C, and D ($t_{\mathrm{AF}} = 5$ nm) for the investigated reversal fields H_α. Corresponding Lorentzian fits $\mathcal{L}(H_\alpha, H^0_\alpha, \Delta H_\alpha, \mathcal{A})$ are represented with black solid lines. Respective integrated distributions $\mu(H_{\mathrm{i}})$ of the interaction field H_{i} with respect to spot N indicated in Fig. 3 are given as filled curves in the background.

$$\mathcal{L}\left(H_\alpha, H^0_\alpha, \Delta H_\alpha, \mathcal{A}\right) = \frac{2\mathcal{A}}{\pi} \frac{\Delta H_\alpha}{4\left(H_\alpha - H^0_\alpha\right)^2 + {\Delta H_\alpha}^2} \tag{9}$$

with the shift H^0_α from the center and the derivable peak height $\mathcal{L}_{\mathrm{max}} = 2\mathcal{A}/\pi\Delta H_\alpha$ are fitted to $\mathrm{d}M_{\mathrm{VMD}}(H_\alpha)/2$ (Fig. 5). The derived parameters as different measures for the VMD are given in Table II for measured and simulated FORCs with different thicknesses t_{F}, t_{AF} and parameters K_{F}, p_{III}, respectively.

$\mathrm{d}M^{\mathrm{max}}_{\mathrm{VMD}}/2$ is significantly higher for $t_{\mathrm{AF}} = 5$ nm and for $p_{\mathrm{III}} = 0.25$ in comparison to $t_{\mathrm{AF}} = 30$ nm and $p_{\mathrm{III}} = 0.8$, respectively, in which cases $M^{\mathrm{max}}_{\mathrm{VMD}}/2 \leqslant 0.04$. $\mathrm{d}M^{\mathrm{max}}_{\mathrm{VMD}}/2$

TABLE II. Derived values for $\mathrm{d}M^{\mathrm{max}}_{\mathrm{VMD}}/2$ as well as fit parameters $\mathcal{A}$ and ΔH_α from Lorentzian fits as well as the peak height $\mathcal{L}_{\mathrm{max}}$ for all investigated thicknesses $t_{\mathrm{F}} = 5$, 7.5, and 10 nm and $t_{\mathrm{AF}} = 5$ and 30 nm as well as parameters of model study $K_{\mathrm{F}} = 0$, 0.5 and 2 kJ/m^3 and $p_{\mathrm{III}} = 0.25$ and 0.8. Fit parameters are not given for $\mathrm{d}M^{\mathrm{max}}_{\mathrm{VMD}}/2 < 0.05$ or if the Lorentzian fit was not possible.

t_{F} (nm)	t_{AF} (nm)	$\frac{\mathrm{d}M^{\mathrm{max}}_{\mathrm{VMD}}}{2}$	$\mathcal{L}_{\mathrm{max}}$	$\mathcal{A}\left(\frac{\mathrm{kA}}{\mathrm{m}}\right)$	$\Delta H_\alpha\left(\frac{\mathrm{kA}}{\mathrm{m}}\right)$
5	5	0.18	0.18 ± 0.01	0.29 ± 0.01	1.05 ± 0.05
5	30	0.02			
7.5	5	0.78	0.96 ± 0.19	0.44 ± 0.02	0.29 ± 0.05
7.5	30	0.03			
10	5	0.70	0.90 ± 0.21	0.32 ± 0.04	0.23 ± 0.05
10	30	0.04			
$K_{\mathrm{F}}\left(\frac{\mathrm{kJ}}{\mathrm{m}^3}\right)$	p_{III}				
0	0.25	0.44	0.45 ± 0.02	0.71 ± 0.02	1.00 ± 0.03
0	0.80	0.03			
0.5	0.25	0.81	0.85 ± 0.06	0.68 ± 0.02	0.51 ± 0.02
0.5	0.80	0.04			
2.0	0.25	0.97	0.98 ± 0.11	0.34 ± 0.01	0.19 ± 0.01
2.0	0.80	<0.01			

increases for increasing K_F with a maximum for $t_F = 7.5$ nm. The same holds true for the determined peak height $\mathcal{L}_{max}$. The peak area $\mathcal{A}$ shows the same trend for increasing t_F but an inversed trend for increasing K_F, i.e., decreasing $\mathcal{A}$ for increasing K_F. The peak width ΔH_α decreases for increasing t_F and K_F, which is in both cases related to the increase of the field range in which the magnetization reversal happens. This results in a larger range of reversal fields from which VMD can be initialized. The peak height $\mathcal{L}_{max}$ and $dM_{VMD}^{max}/2$ are sensitive to the maximum magnetization decrease upon increasing field, only. The area $\mathcal{A}$ is a compromise between $\mathcal{L}_{max}$ or $dM_{VMD}^{max}/2$ and ΔH_α representing a more general characterizing parameter.

Even if the given measures show trends, which already can be recognized in the FORCs and FORC distributions in Figs. 3 and 4, they represent useful tools in order to detect subtle differences between sets of FORCs showing VMD without necessarily needing to calculate the corresponding FORC distributions. The difference in strength of the VMD between $t_F = 7.5$ and 10 nm for $t_{AF} = 5$ nm cannot be securely quantified via only comparing the FORC distributions or the sets of FORCs in Fig. 3, which is possible with comparing $\mathcal{L}_{max}$, $\mathcal{A}$, and ΔH_α showing larger values in the case of $t_F = 7.5$ nm.

V. CONCLUSION

We investigated major and minor loops of a IrMn/NiFe-bilayer as a prototypical polycrystalline in-plane exchange-biased (EB) system for different antiferromagnetic (AF) and ferromagnetic (F) layer thicknesses by means of magneto-optical Kerr magnetometry and microscopy and mapped the distribution of interaction and coercive fields in the context of the first-order reversal curve (FORC) formalism. Comparing angular-resolved measurements with an extended Stoner-Wohlfarth approach by fitting model calculations to experimental data allowed for disentangling the prevailing anisotropies. The percental contribution of AF grains that mediate the rotatable magnetic anisotropy (RMA) and the unidirectional magnetic anisotropy (UDA) could be extracted and directly correlated to the different AF thicknesses. The corresponding parameters are discussed in the context of the polycrystalline model for EB [20,21,25].

Contrary to the commonly observed monotonous magnetization increase upon increasing external magnetic field, we observed a viscous *decrease* of the magnetization upon *increasing* field starting from negative nonsaturating reversal fields [2,10–12,17]. This phenomenon is pronounced in samples with thin AF layers correlated to a dominating RMA, whereas it is suppressed in the case of a pronounced UDA for thick AF layers. By means of Kerr microscopy it was observed, that the viscous magnetization *decrease* (VMD) is mainly mediated by domain wall motion of domains formed before reaching the respective reversal field. Magnetization reversal by coherent rotation during the course of the VMD could be excluded by vectorial Kerr magnetometry revealing a stable multidomain state if the VMD does not cause the sample to reach negative saturation. Depending on whether the VMD ends in a multidomain state dominated by positive or negative domains, a domination of domain wall motion of decreasing domains over the nucleation of new domains or vice versa could be manifested by the combination of vectorial Kerr magnetometry and microscopy on the loop's branch for increasing fields towards positive saturation.

Simulations of FORCs and corresponding FORC distributions based on a coherent rotation approach in the context of the model for polycrystalline EB could qualitatively reproduce the strongly pronounced VMD for strong RMA and the suppression in the case of a strong UDA as well as the identified features in the experimentally determined distributions. The discussion of the results with respect to the application of the coherent rotation approach highlighted limits of the model regarding the uniformity of the F and the persistent entanglement of its intrinsic uniaxial anisotropy and the RMA, which might be solved in the future by implementing a granular F with interacting F entities.

The present study emphasizes the importance of understanding minor loop behavior especially for systems, which are prone to dynamic changes regarding their intrinsic magnetic anisotropies and microscopic properties depending on the path of the external magnetic driving field. The experimental findings clearly evidence the direct connection between the RMA and the VMD in polycrystalline in-plane EB systems merging similar observations presented in literature [16,17].

ACKNOWLEDGMENTS

We acknowledge funding by the DAAD (Project ID 57392264). Further, we thank Adam Krysztofik for fruitful discussions and for performing VNA-FMR measurements.

[1] R. J. Harrison and J. M. Feinberg, Geochem. Geophys. Geosyst. **9**, Q05016 (2008).
[2] D. T. Quach, D. T. Pham, D. T. Ngo, T. L. Phan, S. Y. Park, S. H. Lee, and D. H. Kim, Sci. Rep. **8**, 4461 (2018).
[3] C. R. Pike, A. P. Roberts, and K. L. Verosub, J. Appl. Phys. **85**, 6660 (1999).
[4] L. Alonso, T. R. F. Peixoto, and D. R. Cornejo, J. Phys. D: Appl. Phys. **43**, 465001 (2010).
[5] J. A. Baldwin and F. Milstein, J. Appl. Phys. **44**, 4739 (1973).
[6] K. O'Grady and S. J. Greaves, J. Magn. Magn. Mater. **138**, L233 (1994).
[7] S. Kobayashi, S. Takahashi, T. Shishido, Y. Kamada, and H. Kikuchi, J. Appl. Phys. **107**, 023908 (2010).
[8] D. Toneto, R. B. Da Silva, L. S. Dorneles, F. Béron, S. Oyarzún, and J. C. Denardin, J. Phys. D **53**, 395001 (2020).
[9] M. Al Mamoori, C. Schröder, L. Keller, M. Huth, and J. Müller, AIP Adv. **10**, 015319 (2020).
[10] X. M. Cheng, V. I. Nikitenko, A. J. Shapiro, R. D. Shull, and C. L. Chien, J. Appl. Phys. **99**, 08C905 (2006).
[11] D. T. Robb, Y. H. Xu, O. Hellwig, J. McCord, A. Berger, M. A. Novotny, and P. A. Rikvold, Phys. Rev. B **78**, 134422 (2008).

[12] A. Talantsev, Y. Lu, T. Fache, M. Lavanant, A. Hamadeh, A. Aristov, O. Koplak, R. Morgunov, and S. Mangin, J. Phys.: Condens. Matter **30**, 135804 (2018).
[13] V. Basso, C. Beatrice, M. LoBue, P. Tiberto, and G. Bertotti, Phys. Rev. B **61**, 1278 (2000).
[14] W. H. Meiklejohn and C. P. Bean, Phys. Rev. **105**, 904 (1957).
[15] F. Radu, A. Westphalen, K. Theis-Bröhl, and H. Zabel, J. Phys.: Condens. Matter **18**, L29 (2006).
[16] J. McCord, R. Mattheis, and D. Elefant, Phys. Rev. B **70**, 094420 (2004).
[17] V. Z. C. Paes, R. F. Lopes, and J. Geshev, Eur. Phys. J. Plus **135**, 714 (2020).
[18] J. Geshev, L. G. Pereira, and J. E. Schmidt, Phys. Rev. B **66**, 134432 (2002).
[19] A. Harres and J. Geshev, J. Phys.: Condens. Matter **24**, 326004 (2012).
[20] N. D. Müglich, A. Gaul, M. Meyl, A. Ehresmann, G. Götz, G. Reiss, and T. Kuschel, Phys. Rev. B **94**, 184407 (2016).
[21] M. Merkel, R. Huhnstock, M. Reginka, D. Holzinger, M. Vogel, A. Ehresmann, J. Zehner, and K. Leistner, Phys. Rev. B **102**, 144421 (2020).
[22] N. P. Aley, G. Vallejo-Fernandez, R. Kroeger, B. Lafferty, J. Agnew, Y. Lu, and K. O'Grady, IEEE Trans. Magn. **44**, 2820 (2008).
[23] N. D. Müglich, M. Merkel, A. Gaul, M. Meyl, G. Götz, G. Reiss, T. Kuschel, and A. Ehresmann, New J. Phys. **20**, 053018 (2018).
[24] D. Mauri, E. Kay, D. Scholl, and J. K. Howard, J. Appl. Phys. **62**, 2929 (1987).
[25] K. O'Grady, L. E. Fernandez-Outon, and G. Vallejo-Fernandez, J. Magn. Magn. Mater. **322**, 883 (2010).
[26] A. E. Berkowitz and K. Takano, J. Magn. Magn. Mater. **200**, 552 (1999).
[27] C. Leighton, M. R. Fitzsimmons, A. Hoffmann, J. Dura, C. F. Majkrzak, M. S. Lund, and I. K. Schuller, Phys. Rev. B **65**, 064403 (2002).
[28] J. G. Hu, G. J. Jin, and Y. Q. Ma, J. Appl. Phys. **94**, 2529 (2003).
[29] J. Zehner, R. Huhnstock, S. Oswald, U. Wolff, I. Soldatov, A. Ehresmann, K. Nielsch, D. Holzinger, and K. Leistner, Adv. Electron. Mater. **5**, 1900296 (2019).
[30] J. McCord, R. Schäfer, K. Theis-Bröhl, H. Zabel, J. Schmalhorst, V. Höink, H. Brückl, T. Weis, D. Engel, and A. Ehresmann, J. Appl. Phys. **97**, 10K102 (2005).
[31] E. Fulcomer and S. H. Charap, J. Appl. Phys. **43**, 4190 (1972).
[32] A. Ehresmann, D. Junk, D. Engel, A. Paetzold, and K. Röll, J. Phys. D **38**, 801 (2005).
[33] F. Radu and H. Zabel, Springer Tracts Mod. Phys. **227**, 97 (2007).
[34] G. Vallejo-Fernandez, N. P. Aley, J. N. Chapman, and K. O'Grady, Appl. Phys. Lett. **97**, 222505 (2010).
[35] G. Vallejo-Fernandez, L. E. Fernandez-Outon, and K. O'Grady, Appl. Phys. Lett. **91**, 212503 (2007).
[36] J. Nogués and I. K. Schuller, J. Magn. Magn. Mater. **192**, 203 (1999).
[37] A. Mougin, T. Mewes, M. Jung, D. Engel, A. Ehresmann, H. Schmoranzer, J. Fassbender, and B. Hillebrands, Phys. Rev. B **63**, 060409(R) (2001).
[38] J. Juraszek, J. Fassbender, S. Poppe, T. Mewes, B. Hillebrands, D. Engel, A. Kronenberger, A. Ehresmann, and H. Schmoranzer, J. Appl. Phys. **91**, 6896 (2002).
[39] P. Kuświk, A. Gaul, M. Urbaniak, M. Schmidt, J. Aleksiejew, A. Ehresmann, and F. Stobiecki, Nanomaterials **8**, 813 (2018).
[40] P. Kuświk, B. Szymański, B. Anastaziak, M. Matczak, M. Urbaniak, A. Ehresmann, and F. Stobiecki, J. Appl. Phys. **119**, 215307 (2016).
[41] M. Vopsaroiu, G. V. Fernandez, M. J. Thwaites, J. Anguita, P. J. Grundy, and K. O'Grady, J. Phys. D **38**, 490 (2005).
[42] J. H. Hsu, A. C. Sun, and P. Sharma, Thin Solid Films **542**, 87 (2013).
[43] S. Nieber and H. Kronmüller, Phys. Status Solidi B **165**, 503 (1991).
[44] J. M. Linke, D. Y. Borin, and S. Odenbach, RSC Adv. **6**, 100407 (2016).
[45] X. Zhao, A. P. Roberts, D. Heslop, G. A. Paterson, Y. Li, and J. Li, J. Geophys. Res. Solid Earth **122**, 4767 (2017).
[46] F. Groß, S. E. Ilse, G. Schütz, J. Gräfe, and E. Goering, Phys. Rev. B **99**, 064401 (2019).
[47] A. J. Newell, Geochem. Geophys. Geosyst. **6**, Q05010 (2005).
[48] S. Ruta, O. Hovorka, P. W. Huang, K. Wang, G. Ju, and R. Chantrell, Sci. Rep. **7**, 45218 (2017).
[49] W. S. Cleveland, J. Am. Stat. Assoc. **74**, 829 (1979).
[50] I. D. Mayergoyz, Phys. Rev. Lett. **56**, 1518 (1986).
[51] W. Daeng-Am, P. Chureemart, A. Rittidech, L. J. Atkinson, R. W. Chantrell, and J. Chureemart, J. Phys. D: Appl. Phys. **53**, 045002 (2020).
[52] M. Goto, H. Tange, and T. Kamimori, J. Magn. Magn. Mater. **62**, 251 (1986).